




Research Article



# Effect of anions on the structural, morphological and dielectric properties of hydrothermally synthesized hydroxyapatite nanoparticles

Lakshmanaperumal Sundarabharathi<sup>1</sup> · Deepalekshmi Ponnamma<sup>2</sup>  · Hemalatha Parangusan<sup>2</sup> · Mahendran Chinnaswamy<sup>3</sup> · Mariam Al Ali Al-Maadeed<sup>4</sup>

Received: 7 July 2019 / Accepted: 27 November 2019 / Published online: 16 December 2019

© The Author(s) 2019 

## Abstract

Synthetic nano hydroxyapatites (HA) have been considered as potential biomaterials for bone tissue engineering applications because of its excellent biological properties. The present work deals with the synthesis of HA nanoparticles from different anion source materials via autoclave assisted hydrothermal method. All the prepared HA nanoparticles were characterized by X-ray diffraction (XRD), Fourier transformation infrared spectra, field emission scanning electron microscopy, energy dispersive spectra and high resolution transmission electron microscopy. The XRD patterns reveal the pure and hexagonal phase structure with smaller crystallite size for HA obtained from various calcium salt precursors. HA particles prepared from nitrate precursors show spherical morphology with 32 nm grain size whereas those derived from the acetate, chloride and egg shell precursors respectively show needle-like, irregular and oval morphology. The effect of different anions on the dielectric properties and alternating conductivity of HA is investigated, as a polarized surface can trigger biological reactions. For the particles obtained from nitrate, acetate, chloride and egg shell precursors respectively give dielectric constant ( $\epsilon'$ ) values of 9.96, 13.22, 9.92 and 10.86 at 5 MHz. The  $\epsilon'$  and dielectric loss ( $\epsilon''$ ) values for the HA nanoparticles decrease with increase in the applied frequency as well. The alternating current conductivity values confirm that the as-synthesized HA samples exhibit insulating behavior. In short this article provides the various applicability of HA particles in optoelectronics and drug delivery.

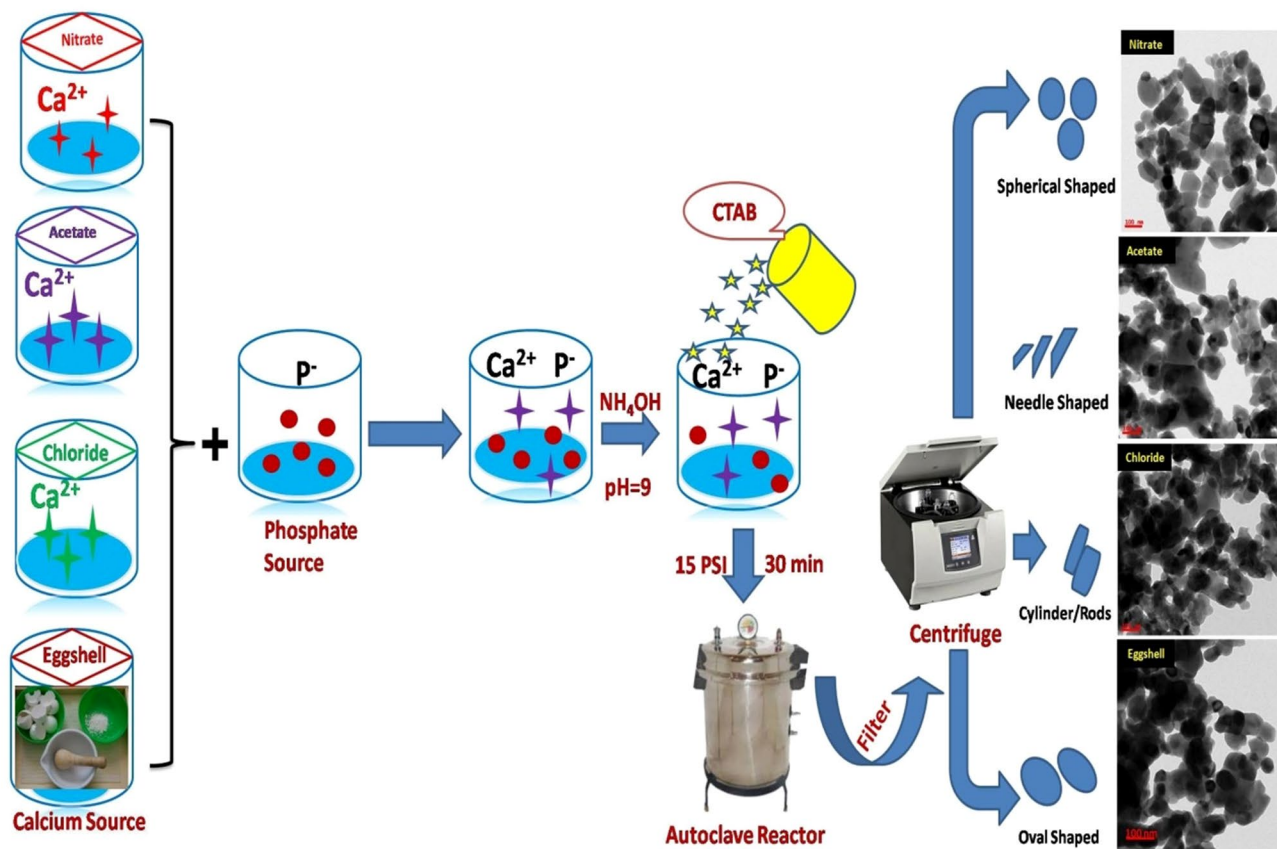
---

✉ Lakshmanaperumal Sundarabharathi, lakshmanphd1201@gmail.com; ✉ Deepalekshmi Ponnamma, lekshmi\_deepa@yahoo.com | <sup>1</sup>Department of Physics, S.S. Duraisamy Nadar Mariammal College, Kovilpatti, Tamilnadu 628 501, India. <sup>2</sup>Center for Advanced Materials, Qatar University, P. O. Box 2713, Doha, Qatar. <sup>3</sup>Department of Physics, Sri Ramakrishna Mission Vidyalaya College of Arts and Science, Coimbatore, Tamilnadu 641 020, India. <sup>4</sup>Materials Science and Technology Program, Qatar University, P. O. Box 2713, Doha, Qatar.



SN Applied Sciences (2020) 2:94 | <https://doi.org/10.1007/s42452-019-1807-3>

Graphic abstract



**Keywords** Hydroxyapatite · Anions · Autoclave assisted · Dielectrics · AC conductivity

**1 Introduction**

Novel bioceramic materials are remarkably developed in recent years due to their significant clinical requirements [1]. Similarly, the demands for advanced biomedical devices, tissue engineering applications and other clinical procedures are growing at an enormous rate. Of the various biomedical issues, the loss of bone tissue due to disease or trauma remains as a major and serious health concern [2, 3]. As far as the orthopedic applications are considered, the hydroxyapatite ((Ca<sub>10</sub>(PO<sub>4</sub>)<sub>6</sub>(OH)<sub>2</sub>), HA) plays a versatile role in bone and hard tissues regenerations, because of its close chemical and physical resemblance to the mineral constituent of human hard tissues [4]. In addition, it shows excellent biocompatibility, bioactivity and osteoconductivity, making it useful for many biomedical applications [5]. Nevertheless, nanotechnology extends its application in many important areas, such as solar cells, battery electrodes, gas sensors, magnetic, optoelectronics devices and photo catalysts [6–8]. However, the commercially available HA is more expensive due

to the use of high purity reagents [9] during the synthesis. Thus the synthetic HA derived from various raw materials including natural sources has superior significance that they inherit variable structural and chemical properties.

Natural sources such as waste egg shell as a source material for HA synthesis offers promising way of nanoparticle synthesis with little environmental hazards. The eggs are used in huge amount in food processing technology and after utilization; the eggshells are disposed as wastes. The eggshell contains calcium carbonate (94%), calcium phosphate (2%), and organic matters (4%) [10] which can be the precursor materials for HA nanoparticles. The synthesized HA generally possesses hexagonal structure containing calcium ions combined with phosphate and hydroxyl ions [11]. The HA is a dielectric material due to this specific ions configuration and improves the electrical properties of its composites. This contributes towards the successful utilization of HA in electronic systems and its electronic properties varies depending on various parameters, such as preparation techniques, calcium/phosphorous (Ca/P) ratios, nonstoichiometry, defects,

crystallite size and the possible surface atmospheric reaction [10]. Therefore, to investigate the electronic structure, it is essential to study the atomic and structural properties of the synthetic HA obtained from different anionic precursors.

Generally, the preparation methods and the conditions of synthesis are crucial factors for manufacturing synthetic HA particles, and they possess major role in chemical as well as structural applications of HA. Therefore, alternative methods and simple techniques are employed to synthesize HA nanoparticles in industrial-scale with good quality, uniformity and perfect crystalline structure [11]. The various synthetic methods used to generate HA nanoparticles include microwave assisted, hydrothermal, sol-gel, micro-emulsion, freezing method, solvothermal, high-gravity precipitation and chemical precipitation methods [11–17]. However, in recent years, autoclave assisted hydrothermal method is also highly employed for the nanoparticle synthesis. This particular method has several eminent advantages, such as high product purity, homogeneous compositions, low synthesis temperature and less required time [18, 19]. Here, the current study addresses synthesizing HA nanoparticles by autoclave assisted hydrothermal method using a chelating agent cetyltrimethylammonium bromide (CTAB). The effects of anions on the crystal structure, morphology, purity and electrical properties of HA nanoparticles are studied elaborately using various analytical techniques. This study helps to identify the perfect anionic modifications on the HA nanoparticles to get maximum efficiency for the generated particles. In addition, the dielectric properties illustrate the possible applications of synthetic HA in energy storing applications.

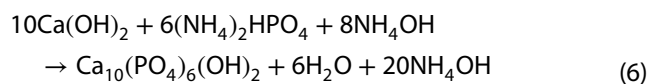
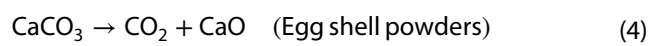
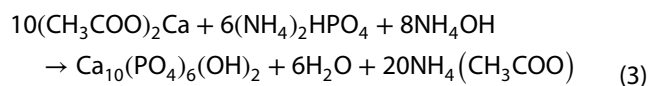
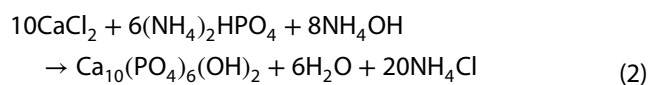
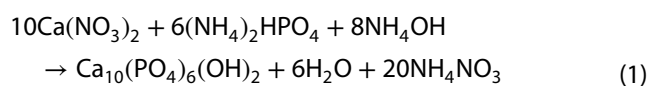
## 2 Experimental details

### 2.1 Preparation of hydroxyapatite nanoparticles

HA nanoparticles were prepared through autoclave assisted hydrothermal method. Different precursor materials such as calcium nitrate, calcium acetate, calcium chloride of analytical grade were obtained from Merck, India. The waste hen eggshells were collected and immersed in boiling water to remove inner membrane and surface contaminants. After drying, they were crushed and powdered using an agate mortar [20]. After, 1.42 g eggshell powder was used as calcium source material for the preparation of HA sample. About 0.5 M calcium salts and 0.3 M diammonium hydrogen phosphate ((NH<sub>4</sub>)<sub>2</sub>HPO<sub>4</sub>) were separately dissolved in 50 ml of deionized water and adjusted the pH to be 9 by adding ammonium hydroxide (NH<sub>4</sub>OH) under constant stirring. For all the samples, the Ca/P molar ratio was maintained at 1.67. Later, the (NH<sub>4</sub>)<sub>2</sub>HPO<sub>4</sub> solution was

slowly added dropwise into the calcium solution, followed by 10 ml 0.1 M CTAB solution and obtained a colloidal suspension with continuously vigorous stirring for 2 h. The resultant milky solution was transferred to polypropylene-capped bottles of 100 ml capacity and then subjected to autoclave reactor with pressure 15 psi for 30 min. After completing the reaction processes, the autoclave-bottles were cooled down to room temperature. The as obtained solutions were then separated by centrifugation and washed several times with distilled water and ethanol to remove impurity ions and subsequently dried at 120 °C for about 3 h in hot air oven, and then calcined at 700 °C for 2 h in a muffle furnace to obtain pure nano HA samples.

The synthesis reaction of HA from different anion precursors can be described as follows:



### 2.2 Characterization of the HA samples

The phase and structural investigation of the HA samples were done by X-Ray Diffractometer (PANalytical model X'PERT-PRO X-ray diffractometer system) equipped with monochromatic CuK $\alpha$  (target) radiation ( $\lambda = 1.5418 \text{ \AA}$ ). The identification of functional groups in the HA samples was done by Fourier transformation infrared (FT-IR) analysis (Nicolet 380 spectrometer using KBr pellet technique) by scanning during the wave number 4000–400 cm<sup>-1</sup>. The surface morphology and elemental composition of the samples were analyzed using field emission scanning electron microscope (FESEM, Zeiss, 6027 Merlin compact) equipped with energy dispersive X-ray (EDS) and high resolution transmission electron microscope (HRTEM, FEI Tecnai G2 S-Twin-D 2087, 200 kV). The dielectric and alternating current conductivity properties were further

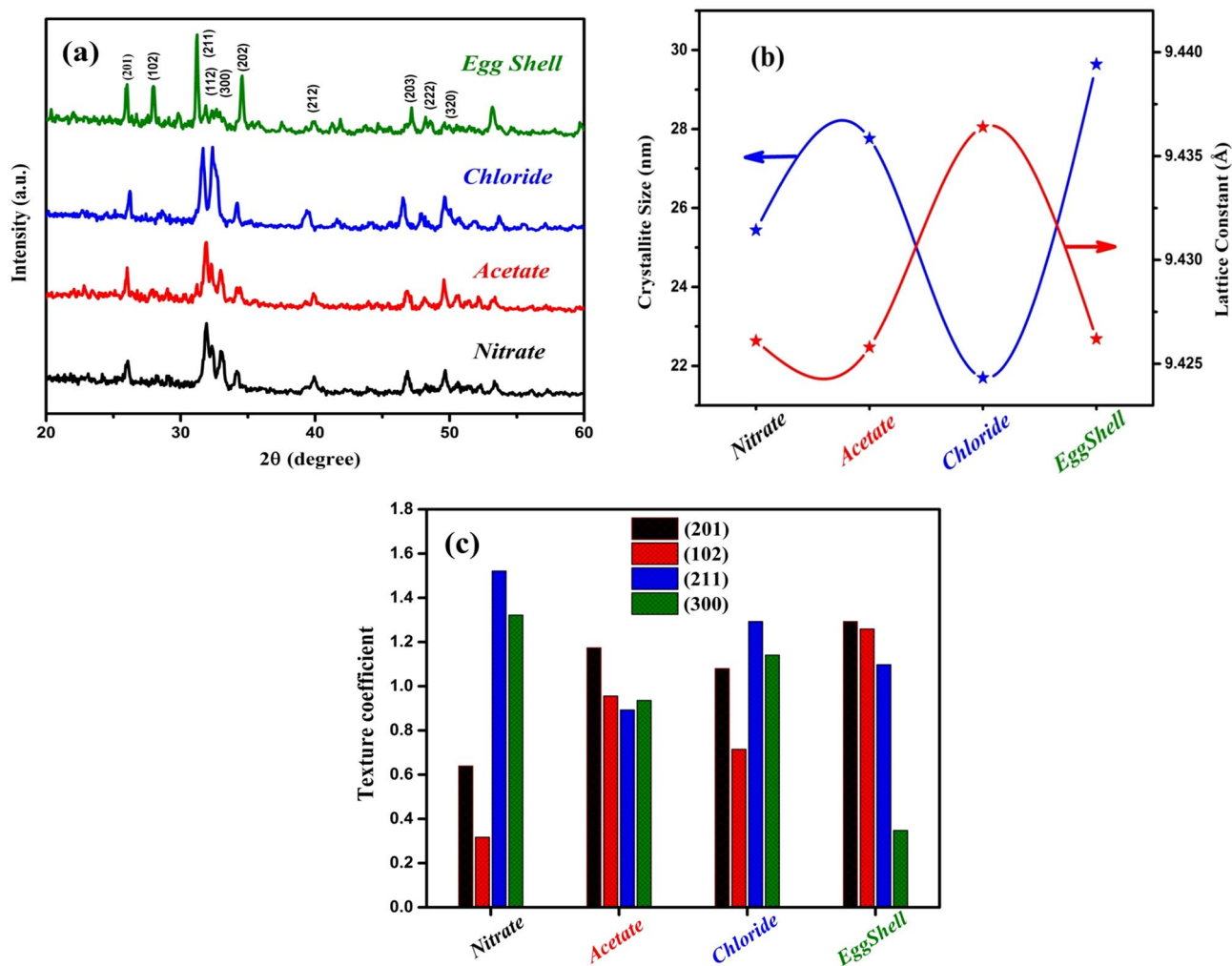


**Fig. 1** **a** XRD patterns of hydroxyapatite (HA) nanoparticles, **b** crystallite size and lattice constants of HA samples and **c** texture coefficient HA samples, synthesized using four different anions

investigated using a HIOKI 3532-50 LCR HiTESTER at room temperature.

### 3 Results and discussion

#### 3.1 XRD analysis

Figure 1a shows the XRD patterns of the HA nanoparticles synthesized using four different calcium precursors by autoclave assisted hydrothermal method (as explained in Eqs. 1, 2, 3 and 6). The typical XRD patterns of all the samples exhibit a hexagonal phase structure of HA, in good agreement with the standard data (JCPDS card No. 09-0432). Major diffraction peaks are observed at 2θ values of 25.9°, 31.9°, 32.5° and 32.9° corresponding to the crystal planes of (201), (211), (112) and (300) respectively. No other extraneous peaks such as β-TCP or α-TCP were

observed besides those of HA phase which suggests the high phase purity of the prepared samples. Presence of sharp diffraction peaks indicate the crystalline nature of the prepared samples. The comparatively higher peak width for the particles prepared from the chloride and nitrate anionic precursors indicates smaller crystallite size and less crystallinity when compared with those samples prepared from acetate and eggshell anions.

The average crystallite size (D) is calculated from the well-known Scherrer's Eq. 7 [21]:

$$D = \frac{0.9\lambda}{\beta \cos \theta} \tag{7}$$

where λ is the wavelength of X-ray (λ=0.154 nm), β is the full-width at half-maximum (FWHM) measured in radian and θ the diffraction angle. The degree of crystallinity (X<sub>c</sub>)

**Table 1** Structural parameters of the as-synthesized HA nanoparticles by autoclave assisted hydrothermal method

Sample code	Lattice parameter (Å)		Lattice distortion c/a	Crystallite size (D) (nm)	Degree of crystallinity ( $X_c$ )	Lattice strain ( $\epsilon$ )	Dislocation density ( $m^{-2}$ )	Specific surface area ( $m^2/g$ )
	a=b	c						
Calcium nitrate	9.4261	6.8762	0.7294	25.44	0.1116	$7.0 \times 10^{-4}$	$1.54 \times 10^{-15}$	103.23
Calcium acetate	9.4258	6.8720	0.7290	27.76	0.1364	$6.7 \times 10^{-4}$	$1.297 \times 10^{-15}$	96.10
Calcium chloride	9.4364	6.9272	0.7340	21.70	0.0686	$9.3 \times 10^{-4}$	$2.123 \times 10^{-15}$	121.33
Calcium eggshell	9.4262	6.8562	0.7273	29.64	0.1669	$6.6 \times 10^{-4}$	$1.13 \times 10^{-15}$	89.68

of the synthesized nanoparticles was also calculated using Eq. 8 [22]

$$X_c = \left(\frac{0.24}{\beta}\right)^3 \tag{8}$$

It is found that the crystallite size and crystallinity calculated using the above equations follow the trend: Calcium Chloride < Calcium Nitrate < Calcium Acetate < Calcium-Eggshell, for various precursors. The two independent factors of lattice strain and small crystallite sizes generally contribute to the peak broadening in the diffraction pattern [23]. Stokes-Wilson equation (Eq. 9) is widely used to determine the lattice strain ( $\epsilon$ ) [24]

$$\epsilon = \frac{\beta}{4 \tan \theta} \tag{9}$$

The total peak broadening is represented by the sum of the contributions of crystallite size and strain present in the material. Assuming that the strain present in the material is uniform, the crystal is supposed to have isotropic nature. The influence of lattice strain values on the XRD peak broadening is clear from the values given in Table 1. A lattice parameter expansion with decreased particle size is attributed to the surface stress, strain and surface defects introduced in the nanocrystalline material during its synthesis [25]. Figure 1b shows the crystallite size and lattice constant values for the HA samples.

From the XRD data, the dislocation density ( $\delta$ ) and specific surface area (S) of the HA particles were also calculated according to the following equation [23, 26]:

$$\delta = \frac{1}{D^2} \tag{10}$$

$$S = \frac{(6 \times 10^3)}{D\rho} \tag{11}$$

Based on all these parameters (Table 1) it is observed that the samples prepared from chloride and nitrate precursors show more variation from the crystalline parameter like dislocation density, specific surface area and lattice

distortion values compared to the samples obtained from acetate and eggshell precursors due to their lower crystallite size (Table 1). In other words, the samples prepared from chloride and nitrate ions show high specific surface area with lower crystallite size whereas samples synthesized from acetate and eggshell exhibit lower specific surface area with increased crystallite size. In addition, the preferential orientation of HA samples prepared from different precursors is quantitatively analyzed by texture coefficient values as illustrated in Fig. 1c. The texture coefficient values indicate the preferential orientation of HA crystallites produced from chloride and nitrate precursors, by their (211) and (300) crystal planes, whereas it changes to (201) in the acetate and eggshell anions. It is worth mentioning that the value of texture coefficient in (h k l) planes, greater than one indicates the progressive orientation of large proportion of crystallites towards a particular plane [27]. Thus, the coefficient exhibits different preferential orientation for calcium apatite crystallites due to the variation in the ionic environment. Thus it is clear that the peak broadening (small crystallite size) effect intimately relates with the preferential orientation.

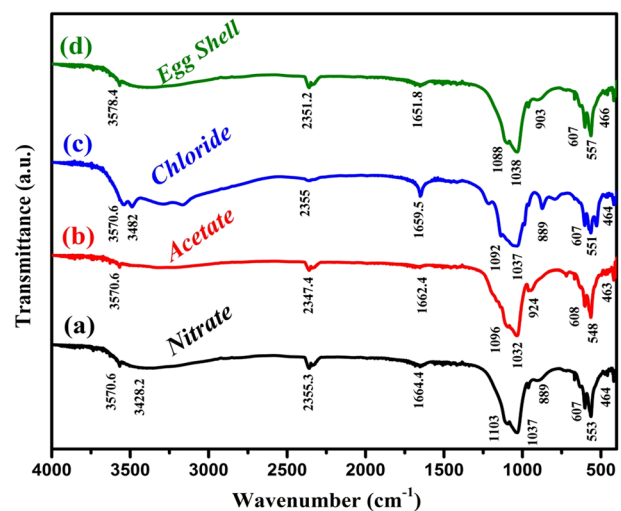


**Fig. 2** FTIR spectra of hydroxyapatite (HA) nanoparticles derived from Nitrate, Acetate, Chloride, and Egg shell precursors

### 3.2 Functional group analysis

Functional groups of HA nanoparticles synthesized with different anions were evaluated by FT-IR (Fig. 2) spectral data. Apatite spectra show the fundamental vibration modes of  $\text{PO}_4$  groups in the apatite structure at about 464, 553, 607, 924, and  $1030\text{--}1100\text{ cm}^{-1}$  [28] wavenumbers. The absorption peak occurred at  $3570\text{ cm}^{-1}$  is associated to the O-H stretching vibration of interlayer water molecules and H-bonds of hydroxyl group. The bands at  $1664\text{ cm}^{-1}$  and  $3428\text{ cm}^{-1}$  attribute to the bending mode of H-O-H vibration coming from the absorbed water molecules [18, 29]. The entire FT-IR spectra show the presence of  $\text{CO}_2$  peak at  $2355\text{ cm}^{-1}$  indicating the involvement of atmospheric gas during the stages of sample preparation. The sharp phosphate bands ( $850\text{--}1050\text{ cm}^{-1}$ ) observed for the samples prepared from nitrate, acetate and egg shell precursors vary from those obtained from chloride due to the fast reaction between precipitant and precursor, and also due

to the high degree of crystallinity. The significant broadening of both these  $-\text{PO}_4$  stretching band and  $-\text{OH}$  stretching bands ( $3000\text{--}3600\text{ cm}^{-1}$ ) of chloride ions when compared with other spectra is an indicator of small crystallite size and crystallinity. Thus the FT-IR result is in good agreement with the XRD analysis (Table 1). The highly sensitive FT-IR spectral results thus reveal the absence of any CTAB molecules in the prepared samples as well.

### 3.3 Morphological analysis

The structural morphology of the HA nanoparticles synthesized with different anionic precursors are investigated by FESEM as shown in Fig. 3a–d. The FESEM micrographs suggest the influence of different anions on the HA particle morphology. The sample prepared from the nitrate precursor (Fig. 3a) shows spherical shaped non-uniform nanostructure with an average grain size of 32 nm. Whereas, the formation of aggregates with needle shaped nanoparticles

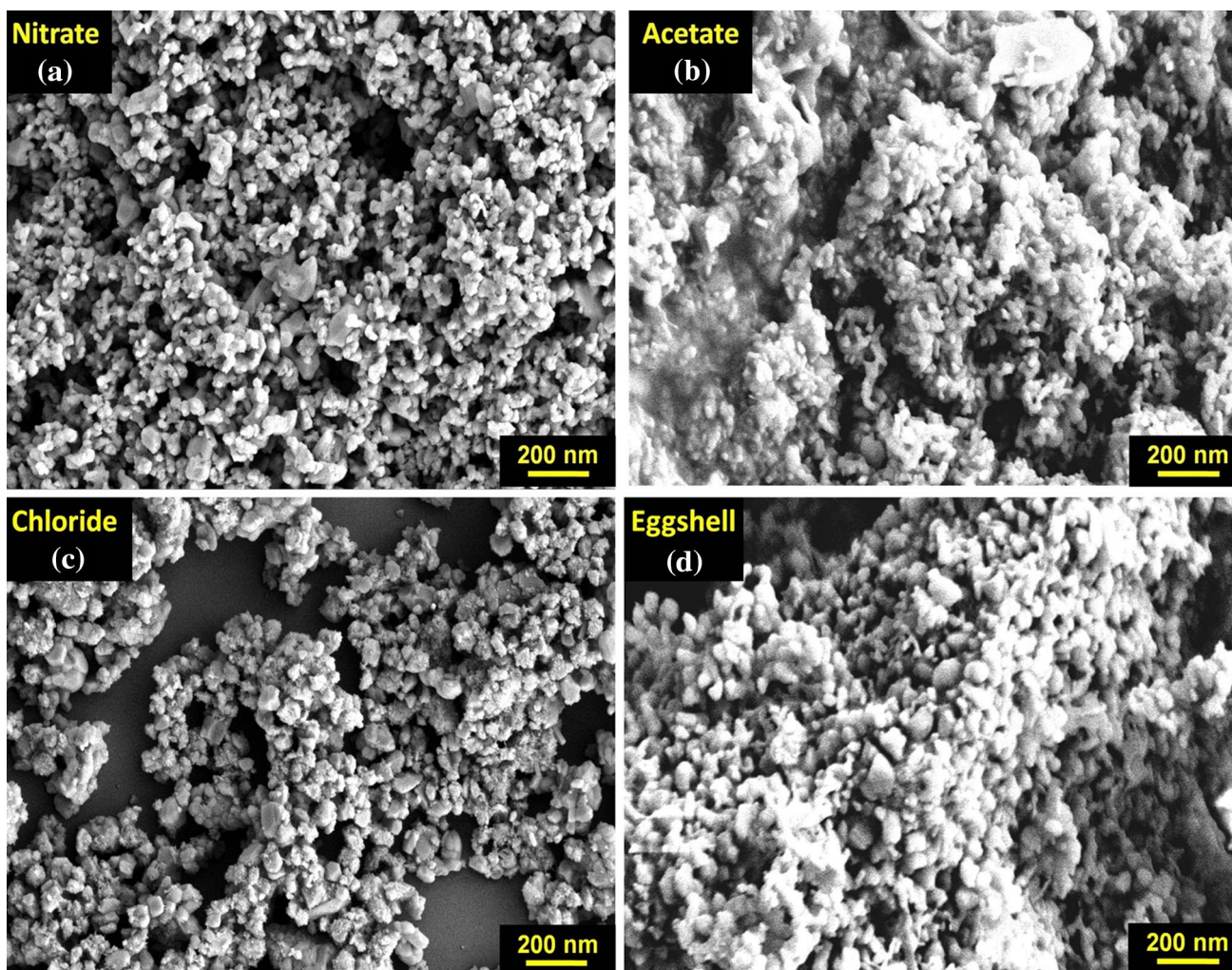
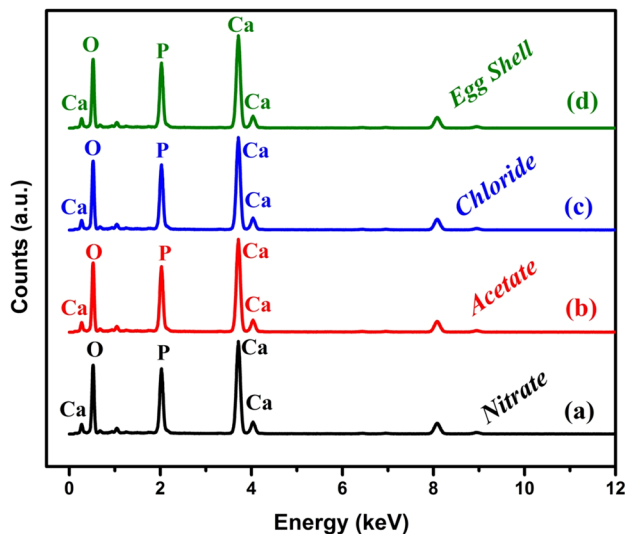


Fig. 3 FESEM surface morphology of HA nanoparticles prepared out of different anions **a** nitrate, **b** acetate, **c** chloride, and **d** egg shell



**Fig. 4** EDS spectra of HA samples prepared out of different anionic precursors

**Table 2** The effect of different anion on Ca: P molar ratio for all the HA samples

Samples	O (at.%)	Ca (at.%)	P (at.%)	Ca/P molar ratio
Calcium nitrate	59.78	24.99	15.23	1.640
Calcium acetate	59.74	25.03	15.23	1.643
Calcium chloride	59.46	25.22	15.32	1.646
Calcium eggshell	59.10	25.44	15.46	1.645

is observed for those samples prepared from acetate precursor. The sample prepared from chloride consists of agglomerated irregular shaped discrete nanoparticles. Moreover, the morphology of the sample prepared from eggshell shows agglomerated nature with oval shaped nanoparticles of average grain size 44 nm (Fig. 3d). The CTAB used is considered as a chelating agent because of its charge and stereochemistry properties. In an aqueous solution, the CTAB would ionize completely and result in a form of cation with tetrahedral structure. Meanwhile, the  $-\text{PO}_4$  anions in HA site also possesses a tetrahedral structure. Hence, the CTAB is capable to regulate the crystallization process [30]. However, the CTAB does not prevent the formation of agglomerates upon mixing the sources of Ca and P.

The energy dispersive spectroscopy (EDS) spectra evidence the presence of Ca, P and O in the HA samples prepared out of different anionic precursors as depicted in Fig. 4. It is further confirmed that, no impure elements are present in HA structure. The elemental composition and Ca: P molar ratio of the samples are summarized in Table 2. The molar ratio of Ca: P is nearly equal to the theoretical

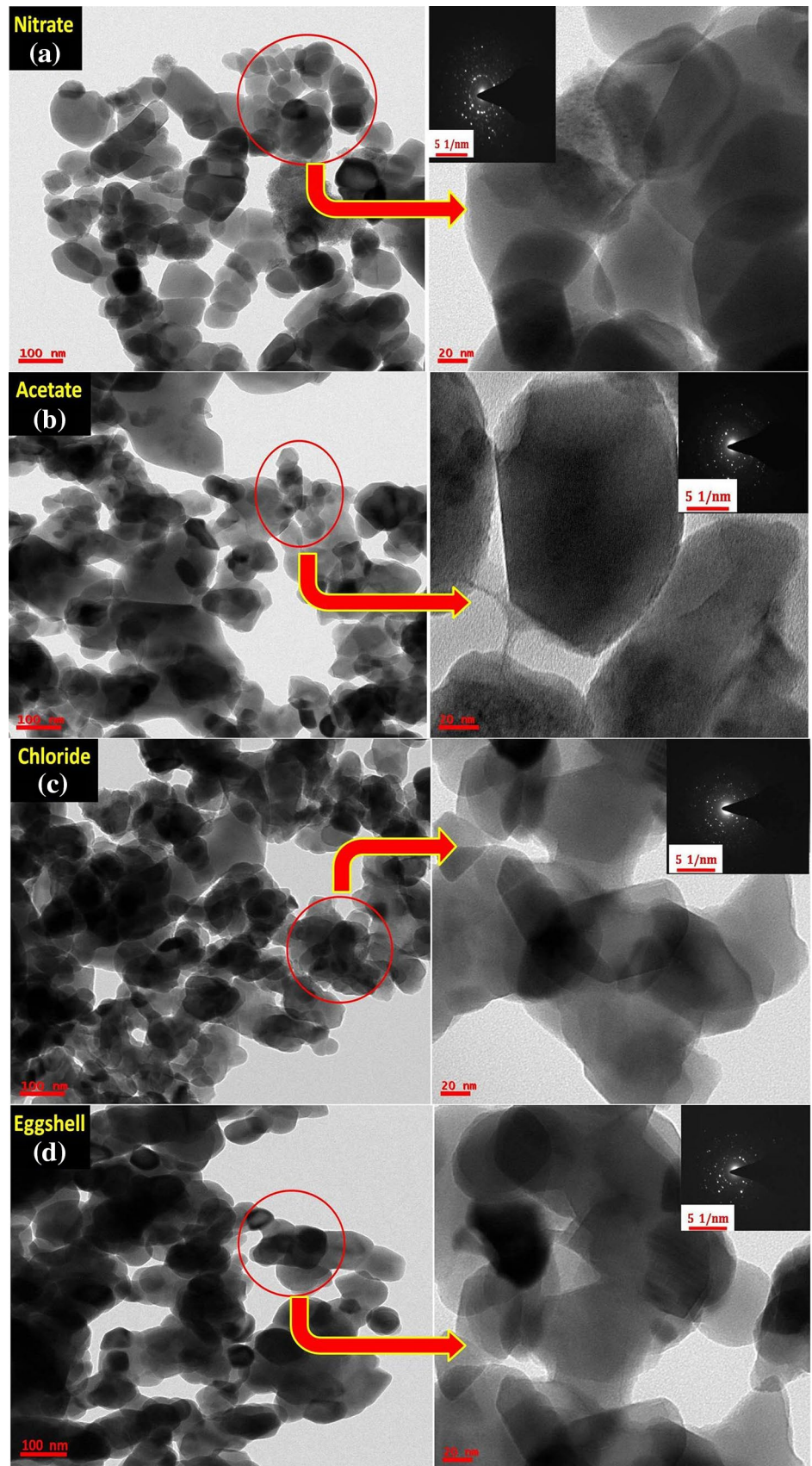
value 1.66, confirming is the presence of no extraneous phase such as  $\alpha$ -TCP or  $\beta$ -TCP in the samples. This result is in good agreement with the observations done from XRD.

To further investigate the interior morphology and size of HA nanoparticles, HRTEM micrographs are used as shown in Fig. 5a–d. The typical nitrate sample consists of elongated spherical shaped nanoparticles with a size below 50 nm. Most of the particles were well separated although some of the particles are loosely aggregated as represented in the enlarged Fig. 5a. The micrograph obtained for the sample prepared from acetate precursor is shown in Fig. 5b which demonstrates the formation of needle shaped particles with an average size 60 nm. Figure 5c shows the chloride sample consisting of non-uniform aggregates of rod like nanoparticles. This involves nucleation, growth and coagulation process, all of which are induced significantly by the chloride salt during reaction. Samples prepared from eggshell demonstrate elongated spherical or oval shape as shown in Fig. 5d. Since the particle size and shape varies based on the precursor anions, it is expected that the anionic environments during the hydrothermal synthesis influence the morphological development of the HA nanoparticles [31]. In short, the morphological highlights of the autoclave mediated apatite nanostructures are much affected by the involved anions and synthesis conditions.

The selected area diffraction patterns exhibit crystallographic direction as shown (insert in TEM). The diffraction spot confirms the crystalline index of the formed nanoparticles with high degree of polycrystalline nature [32]. The TEM-SAED results are also in well consistent with the XRD and FESEM results.

Zeta potential analysis is further carried out to confirm the differently charged sample surfaces of HA nanoparticles [33] as shown in Fig. 6. The results observe the influence of surface charge of the nano HA lattice on the different anion precursors. All HA samples exhibit a negative zeta potential in water at pH 7.4. The potential value obtained for HA between  $-7.6$  and  $-6.2$  mV, is consistent with previous studies [34, 35]. As size decreased, the zeta potential value increased. It can be clearly mentioned that samples prepared from the chloride and nitrate precursors respectively show the zeta potential at  $-6.25$  and  $-6.8$  mV with lower crystallite size of 21.7 nm and 25.44 nm. Whereas the samples synthesized from the acetate and eggshell exhibit lower zeta potentials of  $-7.4$  and  $-7.6$  mV, respectively related to the crystallite sizes 27.76 nm and 29.64 nm. The increased zeta potential confirms the surface structure of the nano HA is being affected by lower crystallite size. This observation is in good agreement with the XRD results.

**Fig. 5** TEM micrographs and the corresponding SAED patterns (shown as an inset) of HA samples synthesized from **a** nitrate, **b** acetate, **c** chloride, and **d** egg shell precursors





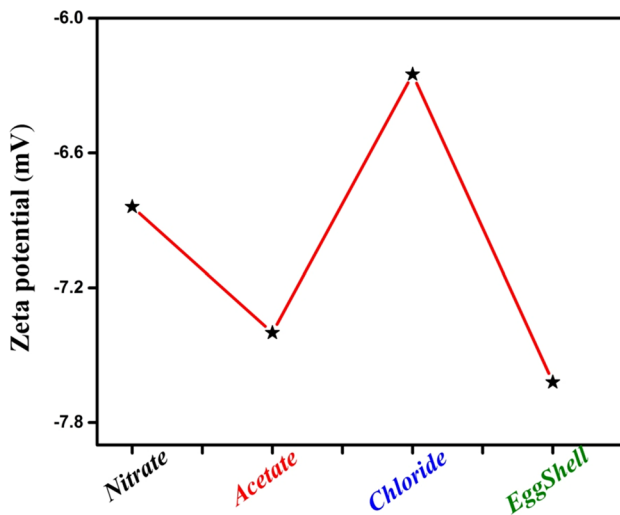


Fig. 6 Zeta potentials analysis of HA nanoparticles prepared out of different anions in aqueous solutions at pH 7.4

### 3.4 Dielectric and AC conductivity of the samples

The improved electrical properties of bioceramic nanomaterials play crucial role in biomedical applications. The dielectric properties of HA nanomaterials are associated with its polarization, as the biological effect can be enhanced on a typical polarized surface. The induced polarization helps to regenerate bone tissues in both in vitro and in vivo [36] experiments. The dielectric real part,  $\epsilon'$  is attributed to the dielectric constant and the imaginary part  $\epsilon''$  to the dielectric loss. The  $\epsilon'$ ,  $\epsilon''$  and the real part of AC conductivity ( $\sigma_{ac}$ ) are calculated by the following relations [37]:

$$\epsilon^* = \epsilon' - i\epsilon'' \tag{12}$$

$$\epsilon' = \frac{C_p t}{\epsilon_0 A} \tag{13}$$

$$\epsilon'' = \frac{G_c t}{\epsilon_0 A \omega} \tag{14}$$

$$\sigma_{ac} = 2\pi f \epsilon_0 \epsilon' \tan \delta \tag{15}$$

where  $\epsilon_0$  is the permittivity of free space charge ( $\epsilon_0 = 8.854 \times 10^{-12}$  F/m),  $A$  is the area of the electrode,  $t$  is thickness of the sample,  $\tan \delta$  is the tangent loss factor ( $\tan \delta = \epsilon''/\epsilon'$ ),  $C_p$  and  $G_c$  are the capacitance and conductance,  $f$  is frequency of applied ac field and  $\omega = 2\pi f$  is the angular frequency. In our experiments, the dielectric properties of the HA nanoparticles synthesized using four different calcium precursors are measured as a function of frequency. The obtained  $\epsilon'$  plots of the HA nanoparticles

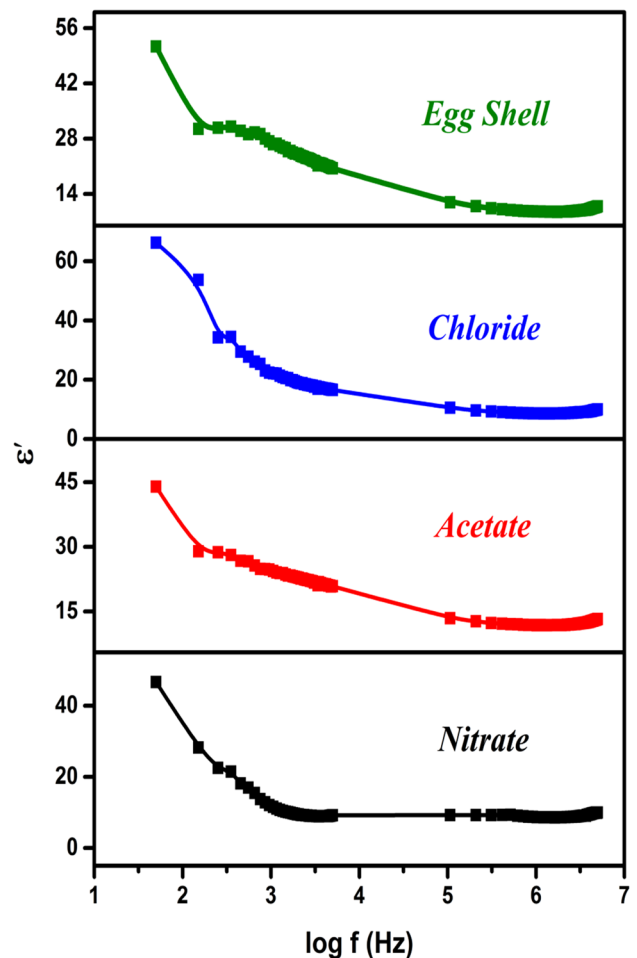


Fig. 7 Dielectric constant ( $\epsilon'$ ) as a function of frequency plots for the HA samples

are shown in Fig. 7. It is observed that the  $\epsilon'$  decreases with the applied frequency of the electric field and the decrease in it is due to the change in the dielectric polarization. The HA nanostructure consists of an array of calcium ions combined with phosphate and hydroxyl ions. At lower frequencies, these ions oscillate when the natural frequency of  $\text{OH}^-$  bound charge is equal to frequency of applied AC field. The oscillations of dipole moments cause a change in  $\epsilon'$  at lower frequency. With different  $\text{Ca}^{2+}$  ions from various precursors, the relative permittivity  $\epsilon'$  is increased

Table 3 The dielectric constant ( $\epsilon'$ ) values of the HA samples at different frequencies

Sample	$\epsilon'_{1 \text{ kHz}}$	$\epsilon'_{100 \text{ kHz}}$	$\epsilon'_{1 \text{ MHz}}$	$\epsilon'_{5 \text{ MHz}}$
Calcium nitrate	11.52	9.20	8.65	9.96
Calcium acetate	24.36	13.39	11.75	13.22
Calcium chloride	22.15	10.51	8.59	9.92
Calcium eggshell	26.56	11.89	9.55	10.86

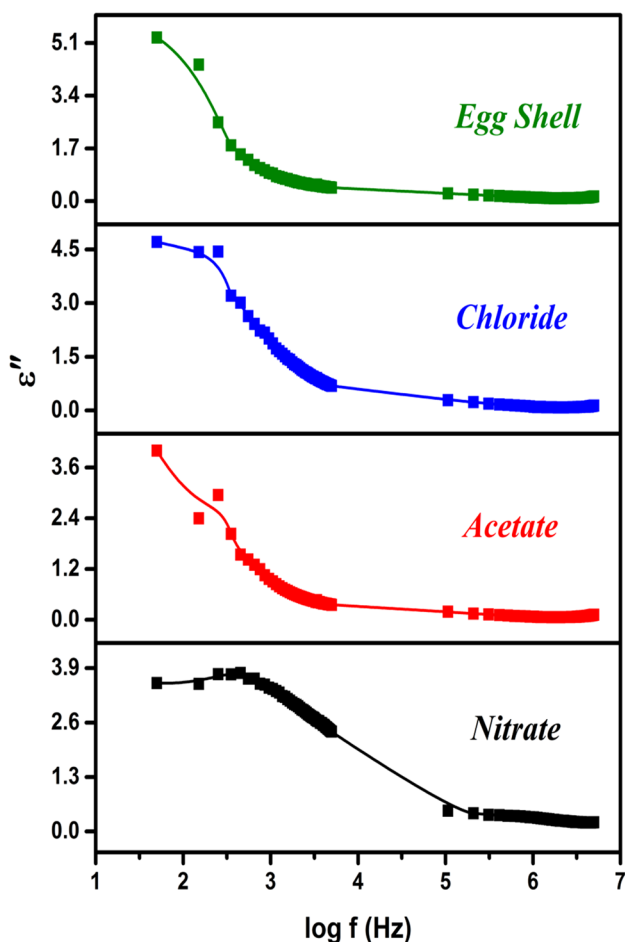


Fig. 8 Dielectric Loss ( $\epsilon''$ ) as a function of frequency plots for the HA samples

Table 4 The dielectric loss ( $\epsilon''$ ) values of the HA samples at different frequencies

Sample	$\epsilon''_{1\text{kHz}}$	$\epsilon''_{100\text{kHz}}$	$\epsilon''_{1\text{MHz}}$	$\epsilon''_{5\text{MHz}}$
Calcium nitrate	3.40	0.490	0.33	0.21
Calcium acetate	0.90	0.187	0.07	0.11
Calcium chloride	1.87	0.283	0.09	0.13
Calcium eggshell	0.88	0.245	0.11	0.14

whereas the crystallite size is decreased. This indicates that there is an inversely proportional relation between the relative permittivity and crystallite size. The influence of various anions changes the relative permittivity and in turn, the crystallite size [38, 39]. The change in  $\epsilon'$  values are also represented in Table 3. At 5 MHz, the calculated values of  $\epsilon'$  are 9.96, 13.22, 9.92 and 10.86 respectively for samples prepared from nitrate, acetate, chloride and egg

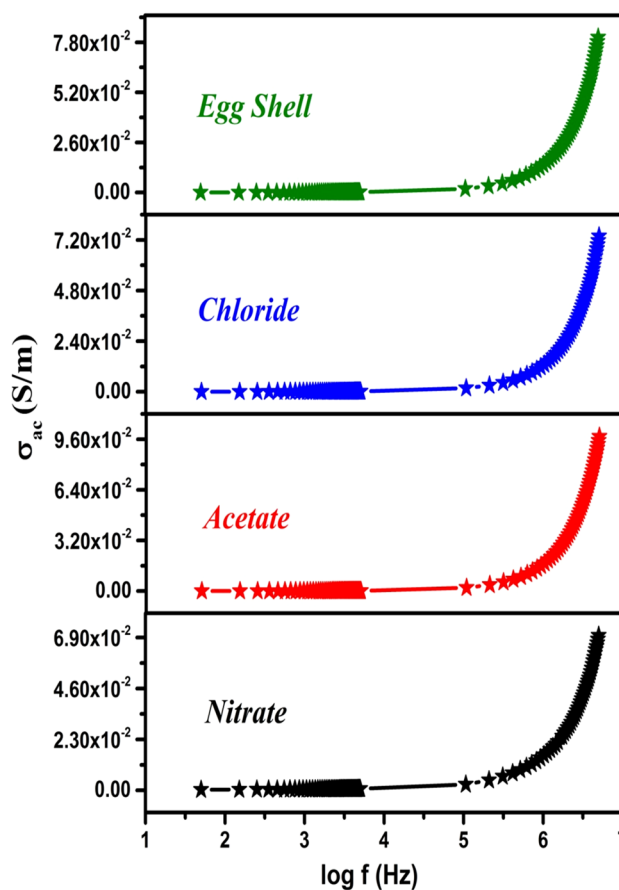


Fig. 9 Alternating current conductivity ( $\sigma_{ac}$ ) versus frequency plots of the as-synthesized HA samples

shell precursors. The obtained results are in good agreement with the previously reported case of Kaygili *et al.* [40, 41]. The larger decrease in  $\epsilon'$  value for the sample obtained from chloride anion is due to the change in ionic polarization. The crystallinity can change the ionic polarization of HA and thus,  $\epsilon'$  is decreased [41].

Figure 8 shows the variations in  $\epsilon''$  values observed for the HA samples. The  $\epsilon''$  spectra of HA samples was also decreased by increasing the applied frequency. No significant change in  $\epsilon''$  value is observed at 5 MHz frequency for all HA nanoparticles prepared with different anions as shown in Table 4. The reduction in  $\epsilon''$  values is due to the migration of ions in all the samples.

Figure 9 shows the AC conductivity of HA nanoparticles prepared from different anionic precursors as a function of frequency. The alternating electrical conductivity ( $\sigma_{ac}$ ) gradually increases with increasing frequency at room temperature for all the HA samples and obeys the universal power law [40]. However in order to confirm the conductivity mechanism of the samples, the well-known Jonscher relation [42] is used as follows.

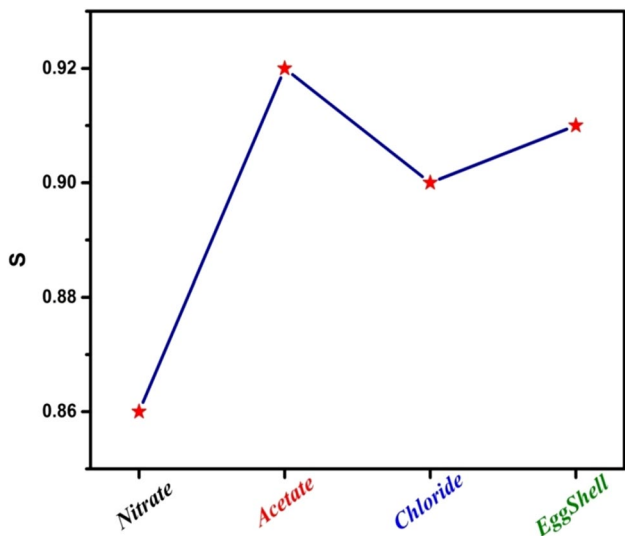


Fig. 10 The plots of frequency exponent (s) value for the HA samples

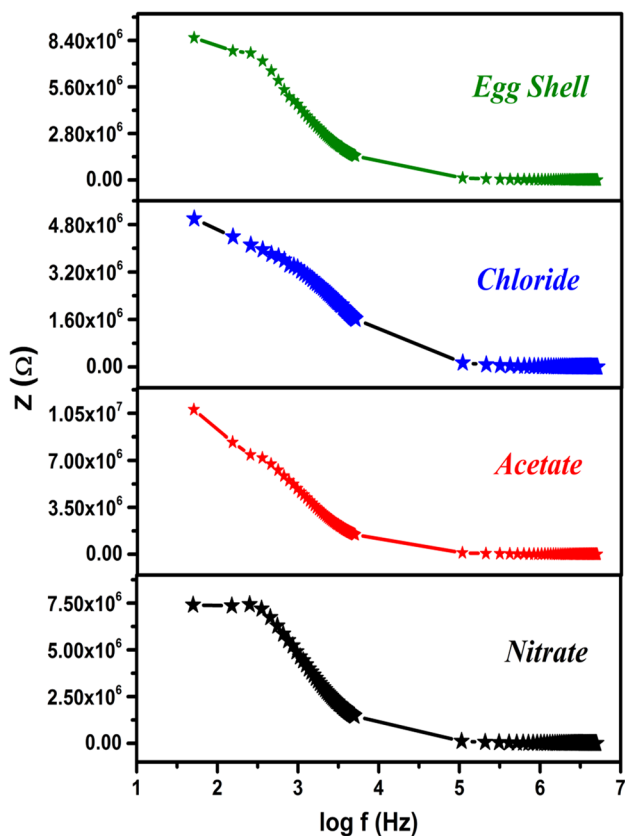


Fig. 11 The plots of impedance (Z) versus frequency for the HA samples

$$\sigma_{ac} = \sigma_{dc} + B\omega^s \tag{16}$$

where  $\sigma_{dc}$  is the direct current conductivity, B is a constant,  $\omega$  is the angular frequency and s is an exponent. The frequency exponent (s) measured from the slope of  $\log \sigma_{ac}$  versus  $\log 2\pi f$  and was respectively found to be 0.86, 0.92, 0.90, and 0.91 for nitrate, acetate, chloride and eggshell based HA nanoparticle (Fig. 10).

The s values for all samples are less than one, suggesting the direct current conductivity of HA samples at room temperature that cannot be measured [43]. The slightly higher s values for the samples prepared from acetate and egg shell precursors become higher insulating with respect to nitrate and chloride based samples. The result suggests that the entire samples follow alternate current conductivity mechanism, i.e. the electron or hole hopping from one charged defect site to another [41]. The plots of resistance versus frequency for the HA samples are shown in Fig. 11. The measured resistance values for all samples range between  $10^6$  and  $10^7 \Omega$ , and this value corresponds to the lower electronic conduction behavior of all the samples prepared from different anions.

Complex impedance spectrum is used to investigate the transport properties of HA nanoparticles at different frequency range. The impedance (Z) is a complex number and is represented by a real part Z' gives resistive and an imaginary part Z'' provide reactive with the formula

$$Z = Z' - iZ'' \tag{17}$$

The room temperature complex impedance spectra for the HA samples prepared out of different anionic precursors are depicted in Fig. 12. Cole–Cole plots typically consist of one spike with semi-circle, which indicates the parallel combination of resistance and capacitance connected with series of one capacitance [44, 45]. The bulk resistance of HA is determined from the intercept on the Z' axis at the

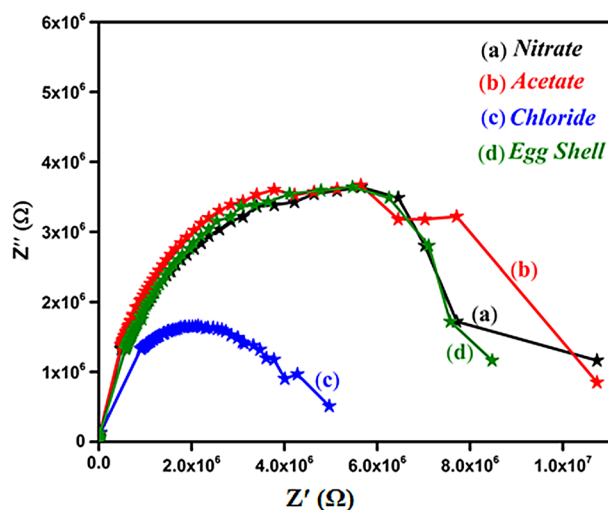


Fig. 12 The complex impedance spectra of the HA nanoparticles prepared out of different anionic precursors

low frequency end of the parabola in Cole–Cole plots. The semi-circle curves are depressed and that their centers are shifted down to the  $Z'$  real axis showing a non-Debye type of relaxation. All the above findings indicate that the use of different  $\text{Ca}^{2+}$  cation precursors influence the dielectric properties of finally produced HA nanoparticles.

## 4 Conclusions

In summary, the autoclave assisted hydrothermal method can be successfully utilized to synthesize pure HA nanoparticles using different calcium precursor materials with Ca: P molar ratio of 10:6. The influence of different anionic precursors on the structural, morphological and dielectric properties of HA nanoparticles were examined utilizing various analytical techniques. The crystallite size, crystallinity and lattice parameters of the HA samples showed appreciable variations depending on the different anionic precursors and this is much evident from the XRD analysis. The FESEM and TEM micrographs illustrate the formation of spherical and oval shaped nanostructures with an average size of 22–60 nm in all HA samples. The purity of the final products and the Ca: P molar ratio were confirmed by FT-IR and EDS spectral studies. The alternating conductivity ( $\sigma_{ac}$ ) was gradually increased with an increasing frequency at room temperature for all the HA samples, and the variations follow universal power law behavior. The HA nanoparticles prepared from nitrate and chloride anions could be used for optoelectronic and drug delivery applications due to its small crystallite size, high specific surface area and high  $\epsilon'$ . According to the data presented from eggshell sample, no significant changes were observed for the structural, purity and dielectric properties. Thus, HA samples with better properties accomplished by autoclave mediated hydrothermal synthesis can be served as better biomaterials in biomedical industry.

**Acknowledgements** Open access funding provided by the Qatar National Library.

## Compliance with ethical standards

**Conflict of interest** The authors declare that they have no conflict of interest.

**Open Access** This article is licensed under a Creative Commons Attribution 4.0 International License, which permits use, sharing, adaptation, distribution and reproduction in any medium or format, as long as you give appropriate credit to the original author(s) and the source, provide a link to the Creative Commons licence, and indicate if changes were made. The images or other third party material in this article are included in the article's Creative Commons licence, unless indicated otherwise in a credit line to the material. If material is not included in the article's Creative Commons licence and your intended

use is not permitted by statutory regulation or exceeds the permitted use, you will need to obtain permission directly from the copyright holder. To view a copy of this licence, visit <http://creativecommons.org/licenses/by/4.0/>.

## References

1. Ingole VH, Hussein KH, Kashale AA, Ghule K, Vuherer T, Kokol V, Chang JY, Ling YC, Vinchurkar A, Dhakal HN, Ghule AV (2017) Ultrasound-assisted green economic synthesis of hydroxyapatite nanoparticles using eggshell biowaste and study of mechanical and biological properties for orthopedic applications. *J Biomed Mater Res Part A* 105:2935–2947
2. Poinern GEJ, Brundavanam RK, Fawcett D (2013) Nanometre scale hydroxyapatite ceramics for bone tissue engineering. *Am J Biomed Eng* 3(6):148–168
3. Murphy MB, Hartgerink JD (2007) Synthesis and in vitro hydroxyapatite binding of peptides conjugated to calcium-binding moieties. *Biomacromol* 8:2237–2243
4. Martins MA, Santos C, Almeida MM, Costa MEV (2008) Hydroxyapatite micro- and nanoparticles: nucleation and growth mechanisms in the presence of citrate species. *J Colloid Interface Sci* 318:210–216
5. Gopi D, Ramya S, Rajeswari D, Karthikeyan P, Kavitha L (2014) Strontium, cerium co-substituted hydroxyapatite nanoparticles: synthesis, characterization, antibacterial activity towards prokaryotic strains and in vitro studies. *Colloids Surf A Physicochem Eng Asp* 451:172–180
6. Kim TG, Park B (2005) Synthesis and growth mechanisms of one-dimensional strontium hydroxyapatite nanostructures. *Inorg Chem* 44(26):9895–9901
7. Wang Y, Chen J, Wei K, Zhang S, Wang X (2006) Surfactant-assisted synthesis of hydroxyapatite particles. *Mater Lett* 60(27):3227–3231
8. He QJ, Huang ZL (2007) Controlled growth and kinetics of porous hydroxyapatite spheres by a template-directed method. *J Cryst Growth* 300(2):460–466
9. Krishna DSR, Siddharthan A, Seshadri SK, Kumar TSS (2007) A novel route for synthesis of nanocrystalline hydroxyapatite from eggshell waste. *J Mater Sci Mater Med* 18(9):1735–1743
10. Rivera EM, Araiza M, Brostow W, Castano VM, Diaz-Estrada JR, Hernandez R, Rodriguez JR (1999) Synthesis of hydroxyapatite from eggshells. *Mater Lett* 41(3):128–134
11. Lakshmanaperumal S, Hemalatha P, Ponnamma D, Maadeed MAA, Mahendran C (2018) In-vitro biocompatibility, bioactivity and photoluminescence properties of  $\text{Eu}^{3+}/\text{Sr}^{2+}$  dual-doped nano-hydroxyapatite for biomedical applications. *J Biomed Mater Res Part B Appl Biomater* 106(6):2191–2201
12. Kaygili O, Tatar C, Yakuphanoglu F (2012) Structural and dielectric properties of  $\text{Mg}_3\text{-Ca}_3(\text{PO}_4)_2$  bioceramics obtained from hydroxyapatite by sol–gel method. *Ceram Int* 38:5713–5722
13. Wijesinghe WPSL, Mantilaka MMMGPG, Rajapakse RMG, Pitawala HMTGA, Premachandra TN, Herath HMTU, Rajapakse RPVJ (2017) Urea-assisted synthesis of hydroxyapatite nanorods from naturally occurring impure apatite rocks for biomedical applications. *RSC Adv* 7:24806–24812
14. Andre RS, Paris EC, Gurgel MFC, Rosa ILV, Paiva-Santos CO, Li MS, Varela JA, Longo E (2012) Structural evolution of Eu-doped hydroxyapatite nanorods monitored by photoluminescence emission. *J Alloys Compd* 531:50–54
15. Peng H, Wang J, Lv S, Wen J, Chen JF (2015) Synthesis and characterization of hydroxyapatite nanoparticles prepared by a high-gravity precipitation method. *Ceram Int* 41:14340–14349

16. Stipniece L, Narkevica I, Salma-Ancane K (2017) Low-temperature synthesis of nanocrystalline hydroxyapatite: effect of Mg and Sr content. *J Am Ceram Soc* 100:1697–1706
17. Kaygili O, Keser S, Kom M, Erokşuz Y, Dorozhkin SV, Ates T, Özercan IH, Tatar C, Yakuphanoglu F (2015) Strontium substituted hydroxyapatites: synthesis and determination of their structural properties, in vitro and in vivo performance. *Mater Sci Eng C* 55:538–546
18. Aidin L, Mazloumi M, Mohajerani M, Kajbafvala A, Zanganeh S, Arami H, Sadrnezhad SK (2008) Self-assembly of dandelion-like hydroxyapatite nanostructures via hydrothermal method. *J Am Ceram Soc* 91(10):3292–3297
19. Yan L, Li Y, Deng ZX, Zhuang J, Sun X (2001) Surfactant-assisted hydrothermal synthesis of hydroxyapatite nanorods. *Int J Inorg Mater* 3:633–637
20. Suresh Kumar G, Thamizhavel A, Girija EK (2012) Microwave conversion of eggshells into flower-like hydroxyapatite nanostructure for biomedical applications. *Mater Lett* 76:198–200
21. Lakshmanaperumal S, Mahendran C, Ponnammma D, Hemalatha P, Maadeed MAA (2019) Investigation of antimicrobial properties and in-vitro bioactivity of Ce<sup>3+</sup>-Sr<sup>2+</sup> dual-substituted nano hydroxyapatites. *J Am Ceram Soc* 102:144–157
22. AnuPriya B, Senthilguru K, Agarwal T, Gautham SN, Narayana H, Giri S, Pramanik K, Pal K, Banerjee I (2015) Nickel doped nano hydroxyapatite: vascular endothelial growth factor inducing biomaterial for bone tissue engineering. *RSC Adv* 5:72515–72528
23. Venkateswarlu K, Chandra Bose A, Rameshbabu N (2010) X-ray peak broadening studies of nanocrystalline hydroxyapatite by Williamson-Hall analysis. *Physica B* 405:4256–4261
24. Ahmadi T, Monshi A, Mortazavi V (2014) Synthesis and dissolution behavior of nanosized silicon and magnesium co-doped fluorapatite obtained by high energy ball milling. *Ceram Int* 40:8341–8349
25. Bayal N, Jeevanandam P (2012) Synthesis of CuO@NiO core-shell nanoparticles by homogeneous precipitation method. *J Alloys Compd* 537:232–241
26. Jahana SA, Mollahb MYA, Ahmeda S, Susan MABH (2017) Nano-hydroxyapatite prepared from eggshell-derived calcium-precursor using reverse microemulsions as nanoreactor. *Mater Today Proc* 4:5497–5506
27. Arunkumar P, Ramaseshan R, Dash S, Basu J, Ravindran TR, Balakumar S, Suresh Babu K (2014) Texturing of pure and doped CeO<sub>2</sub> thin films by EBPVD through target engineering. *RSC Adv* 4:33338–33346
28. Mercado DF, Magnacca G, Malandrino M, Rubert A, Montoneri E, Celi L, Prevot AB, Gonzalez MC (2014) Paramagnetic iron-doped hydroxyapatite nanoparticles with improved metal sorption properties. A bioorganic substrates-mediated synthesis. *ACS Appl Mater Interfaces* 6:3937–3946
29. Uysal I, Severcan F, Evis Z (2013) Characterization by Fourier transform infrared spectroscopy of hydroxyapatite co-doped with zinc and fluoride. *Ceram Int* 39:7727–7733
30. Garcia C, Garcia C, Paucar C (2012) Controlling morphology of hydroxyapatite nanoparticles through hydrothermal microemulsion chemical synthesis. *Inorg Chem Commun* 20:90–92
31. Wang Y, Chen JD, Wei K, Zhang SH, Wang X (2006) Surfactant-assisted synthesis of hydroxyapatite particles. *Mater Lett* 60:3227–3231
32. Suresh R, Ponnuswamy V, Sankar C, Manickam M, Venkatesan S, Perumal S (2017) NiO nanoflakes: effect of anions on the structural, optical, morphological and magnetic properties. *J Magn Magn Mater* 441:787–794
33. Deshmukh K, Shaik MM, Ramanan SR, Kowshik M (2016) Self-activated fluorescent hydroxyapatite nanoparticles: a promising agent for bioimaging and biolabeling. *ACS Biomater Sci Eng* 2(8):1257–1264
34. Cai Y, Liu Y, Yan W, Hu Q, Tao J, Zhang M, Shi Z, Tang R (2007) Role of hydroxyapatite nanoparticle size in bone cell proliferation. *J Mater Chem* 17:3780–3787
35. Chen L, Mccrate JM, Lee JC-M, Li H (2011) The role of surface charge on the uptake and biocompatibility of hydroxyapatite nanoparticles with osteoblast cells. *Nanotechnology* 22:105708
36. AlHammad MS (2016) Nanostructure hydroxyapatite based ceramics by sol gel method. *J Alloys Compd* 661:251–256
37. Baris B (2014) Ac conductivity and dielectric spectroscopy studies on tin oxide thin films formed by spray deposition technique. *Physica B* 438:53–59
38. Kaygili O, Dorozhkin SV, Ates T, Yakuphanoglu F (2014) Dielectric properties of Fe-doped hydroxyapatite prepared by sol-gel method. *Ceram Int* 40(7):9395–9402
39. Lakshmanaperumal S, Mahendran C (2018) Structural, dielectric, cytocompatibility, and in vitro bioactivity studies of yttrium and strontium co-substituted nano-hydroxyapatite by sol-gel method. *J Sol-Gel Sci Technol* 88(296):296–308
40. Kaygili O, Dorozhkin SV, Ates T, Gursoy NC, Keser S, Yakuphanoglu F, Selcuk AB (2015) structural and dielectric properties of yttrium- substituted hydroxyapatites. *Mater Sci Eng C* 47:333–338
41. Kaygili O, Ates T, Keser S, Al-Ghamdi AA, Yakuphanoglu F (2014) Controlling of dielectrical properties of hydroxyapatite by ethylenediamine tetraacetic acid (EDTA) for bone healing applications. *Spectrochim Acta Part A Mol Biomol Spectrosc* 129:268–273
42. Jonscher AK (1977) The 'universal' dielectric response. *Nature* 267:673–679
43. Al-Hazmi FE (2016) Synthesis and electrical properties of Bi doped hydroxyapatite ceramics. *J Alloys Compd* 665:119–123
44. Sundaramahalingam K, Vanitha D, Nallamuthu N, Manikandan A, Muthuvinnayagam M (2019) Electrical properties of lithium bromide poly ethylene oxide/poly vinyl pyrrolidone polymer blend electrolyte. *Physica B* 553:120–126
45. Gopi D, Karthika A, Nithiya S, Kavitha L (2014) In vitro biological performance of minerals substituted hydroxyapatite coating by pulsed electrodeposition method. *Mater Chem Phys* 144:75–85

**Publisher's Note** Springer Nature remains neutral with regard to jurisdictional claims in published maps and institutional affiliations.